

RESEARCH

Open Access



Pseudopotential-based discrete unified gas kinetic scheme for modeling multiphase fluid flows

Zeren Yang¹, Sha Liu^{1,2}, Congshan Zhuo^{1,2} and Chengwen Zhong^{1,2*} 

*Correspondence:
zhongcw@nwpu.edu.cn

¹ School of Aeronautics,
Northwestern Polytechnical
University, 127 West Youyi Road,
710072 Xi'an, China

² National Key Laboratory
of Science and Technology
on Aerodynamic Design
and Research, Northwestern
Polytechnical University, 127
West Youyi Road, 710072 Xi'an,
China

Abstract

To directly incorporate the intermolecular interaction effects into the discrete unified gas-kinetic scheme (DUGKS) for simulations of multiphase fluid flow, we developed a pseudopotential-based DUGKS by coupling the pseudopotential model that mimics the intermolecular interaction into DUGKS. Due to the flux reconstruction procedure, additional terms that break the isotropic requirements of the pseudopotential model will be introduced. To eliminate the influences of nonisotropic terms, the expression of equilibrium distribution functions is reformulated in a moment-based form. With the isotropy-preserving parameter appropriately tuned, the nonisotropic effects can be properly canceled out. The fundamental capabilities are validated by the flat interface test and the quiescent droplet test. It has been proved that the proposed pseudopotential-based DUGKS managed to produce and maintain isotropic interfaces. The isotropy-preserving property of pseudopotential-based DUGKS in transient conditions is further confirmed by the spinodal decomposition. Stability superiority of the pseudopotential-based DUGKS over the lattice Boltzmann method is also demonstrated by predicting the coexistence densities complying with the van der Waals equation of state. By directly incorporating the intermolecular interactions, the pseudopotential-based DUGKS offers a mesoscopic perspective of understanding multiphase behaviors, which could help gain fresh insights into multiphase fluid flow.

Keywords: Pseudopotential model, Discrete unified gas kinetic scheme, Multiphase flows, Isotropic interface

1 Introduction

Multiphase fluid flows featured by the simultaneous presence of multiple thermodynamic phases appear ubiquitous in natural environments and industrial engineering practice. An insightful understanding of the multiphase flow dynamics could practically facilitate manufacturing and production activities. As the mechanical behaviors of multiphase flows are too complex to be fully captured by experimental techniques, a series of interface tracking methods including the level-set (LS) method [1], the volume-of-fluid (VOF) method [2] and the phase-field (PF) method [3], coupled with the numerical solution of the Navier-Stokes equation, have been developed to describe the complex behaviors of multiphase fluid flow from a macroscopic perspective [4]. Owing to the

tremendous advances in computing capability, mesoscopic approaches developed upon the kinetic theory offer a penetrating perspective to comprehend the multiphase interactions. By exploring the multiphase behaviors at the mesoscopic level, the mesoscopic approaches fill the gap between the macroscopic descriptions of the multiphase dynamics and microscopic intermolecular actions [5].

Among plenty of kinetic-based mesoscopic approaches, the lattice Boltzmann (LB) method has emerged as an efficient and powerful tool for simulating a wide range of multiphase fluid flows [6–10]. The multiphase LB models developed in the past three decades can be generally classified into four categories: the color-gradient model [11], the phase-field model [12], the free-energy model [13], and the pseudopotential (PP) model [14]. Both the color-gradient model and the phase-field model take two sets of distribution functions, one for the interfacial property and the other for the hydrodynamic property, to depict the multiphase fluid flow. The free-energy model and the pseudopotential model, which mimic the effects of phase interactions by an additional volumetric force, employ a single set of distribution functions to describe the multiphase fluid flow. With such a treatment, the complexity of the computing program gets roughly halved compared to the program implementing the color-gradient or the phase-field model. Moreover, the mass and momentum transport process in the simulations employing the free-energy or the pseudopotential model is accomplished through the migration of identical particles described by the single set of distribution functions, which tends to be more consistent than the transport process exhibited in the simulations utilizing the color-gradient or the phase-field model, where the mass and momentum transport corresponds respectively to the migration of different particles depicted by two individual sets of distribution functions. Owing to the succinct implementation of the pseudopotential model, the pseudopotential LB method has experienced continued prosperity in a wide range of multiphase fluid flows [15–18]. Nevertheless, theoretical foundations of the pseudopotential model have remained the subject of debate since its birth. A major debating issue lies in the thermodynamic inconsistency. He and Doolean [19] first addressed the problem of the thermodynamic inconsistency and provided the simplified form of the pressure tensor induced by the pseudopotential model. Benzi *et al.* [20] identified the complete form of the pressure tensor at the continuum level. Later, Sbragaglia *et al.* [21] discovered that the continuum form of the pressure tensor does not ensure uniqueness due to the arbitrary gauge. Shan [22] further emphasized that the continuum form of the interaction force does not guarantee exact mechanical balance. The pressure tensor constructed on the discrete level should be employed to accurately predict the thermodynamic behaviors of the pseudopotential model. Kuperstokh *et al.* [23] managed to achieve the thermodynamic consistency by introducing a tunable interaction force. To uncover the underlying thermodynamic background, Sbragaglia and Shan [24] derived the free energy functional in terms of the pseudopotential model and established the specific expression of the interaction potential. It turns out that an implementation of the equation of state in the thermodynamic theory would inevitably result in the thermodynamic inconsistency. Thereafter, Li *et al.* [25] explored the mechanical stability solutions in varying conditions and figured out the appropriate parameter value for approximately fulfilling the thermodynamic inconsistency requirement. With a third-order Chapman-Enskog analysis, Huang *et al.* [26] proved that the

classical discrete pressure tensor proposed by Shan [22] remains only conditionally correct. On the contrary, the continuum pressure tensor constructed by considering the third-order isotropic term could accurately predict the thermodynamic behaviors of the pseudopotential model. Despite the tremendous progress achieved by the pseudopotential model in multiphase fluid flow [6, 27], all of the research has been confined within the framework of LB method. Considering its straightforward implementation and excellent capacity, it is tempting to develop pseudopotential-based kinetic schemes that are not restricted by the uniform Cartesian grid for efficient multiphase flow simulation.

Rooted in the kinetic theory, the discrete unified gas kinetic scheme (DUGKS) developed within the finite volume framework suffers from no restriction on grid types [28]. By considering the local Knudsen information in the construction of kinetic flux, DUGKS could accurately depict extensive fluid flows ranging from the continuum regime to the free molecular regime [29]. Over the past decade, DUGKS has demonstrated its excellent capability in modeling compressible flows [30–32], turbulent flows [33–35], solid-fluid flows [36–38], multicomponent gas flows [39, 40], microscale gas flows [41, 42], radiative heat transfer [43, 44], and so forth. For the widespread application of DUGKS, readers are recommended to refer to the review literature provided by Guo and Xu [45]. Despite the tremendous progress made by DUGKS, studies centered on the multiphase fluid flows are rather limited [46, 47]. Moreover, the multiphase model employed in DUGKS is generally limited to the phase-field model [48], where two sets of distribution functions are utilized to separately describe the interface and fluid dynamics. Such a treatment isolates the mass transport from the momentum transport and could induce unphysical phenomena. To avoid this undesirable feature, DUGKS using a single set of distribution functions for multiphase flow simulations should be developed. Very recently, Zeng *et al.* [49] proposed a well-balanced DUGKS for two-phase flows by absorbing the free-energy model [50] into DUGKS. Only a single set of distribution functions has been utilized in their work for the concurrent transport of mass and momentum. Numerical results demonstrated the superior stability and accuracy of DUGKS over that of LB method. Nevertheless, the free-energy model considers the phase interactions through the chemical potential field, which typically belongs to a macroscopic description. To describe the phase interactions at the mesoscopic level, the pseudopotential model that directly mimics the intermolecular interactions is a distinct preference. Considering the excellent performance of DUGKS proved in previous studies [51, 52], as well as the mesoscopic feature of the pseudopotential model, we developed a pseudopotential-based DUGKS for two-phase fluid flows by coupling the pseudopotential model with the Strang-splitting DUGKS. To simulate a realistic two-phase system, the van der Waals equation of state (vdW-EOS) is implemented for the evaluation of bulk pressure. The rest of this paper is organized as follows: Section 2 introduces the Strang-splitting DUGKS and the pseudopotential model. Section 3 presents the numerical results as well as discussions. Section 4 concludes the findings.

2 Numerical methodology

In this section, the macroscopic governing equations are first briefly introduced. Then we offer a detailed explanation of the Strang-splitting discrete unified gas kinetic scheme. The pseudopotential model for DUGKS will be introduced in the final part.

2.1 Macroscopic equations

The macroscopic governing equations recovered by the kinetic equation through the Chapman-Enskog theory read

$$\frac{\partial \rho}{\partial t} + \nabla \cdot (\rho \mathbf{u}) = 0, \tag{1a}$$

$$\frac{\partial(\rho \mathbf{u})}{\partial t} + \nabla \cdot (\rho \mathbf{u} \otimes \mathbf{u}) = -\nabla p + \nabla \left[\mu \left(\nabla \mathbf{u} + (\nabla \mathbf{u})^T \right) \right] + \mathbf{F}_s + \mathbf{G}, \tag{1b}$$

where t represents time, ρ indicates the fluid density, \mathbf{u} denotes the flow velocity, p is the pressure, and μ is the dynamic viscosity. \mathbf{F}_s stands for the volumetric force that mimics the interaction effects between/among different phases whereas \mathbf{G} indicates the gravitational or buoyant force.

2.2 Discrete unified gas kinetic scheme

In present research, the flow field is directly governed by the Boltzmann-BGK equation, which takes the form of

$$\frac{\partial f}{\partial t} + \boldsymbol{\xi} \cdot \nabla_{\mathbf{x}} f = \Omega \equiv -\frac{f - f^E}{\tau}, \tag{2}$$

where $f = f(\mathbf{x}, \boldsymbol{\xi}, t)$ is the distribution function (DF) accounting for the particles residing at position \mathbf{x} with a velocity of $\boldsymbol{\xi}$ at time t , τ is the relaxation time, f^E is the equilibrium distribution function approached by f within each collision. The moments of the distribution function yield the conservative flow variables via

$$\rho = \int f d\boldsymbol{\xi} = \int f^E d\boldsymbol{\xi}, \quad \rho \mathbf{u} = \int \boldsymbol{\xi} f d\boldsymbol{\xi} = \int \boldsymbol{\xi} f^E d\boldsymbol{\xi}. \tag{3}$$

A necessary prerequisite for the numerical evaluation of the moments is the discretization of the velocity space. In present work, the three-point Gauss-Hermite quadrature is employed to determine the discrete particle velocities along each single dimension. In two dimension the discrete velocities can be derived from the tensor product of the single dimensional velocities, which reads

$$\boldsymbol{\xi}_i = \sqrt{3c_s^2} \begin{bmatrix} 0 & 1 & 0 & -1 & 0 & 1 & -1 & -1 & 1 \\ 0 & 0 & 1 & 0 & -1 & 1 & 1 & -1 & -1 \end{bmatrix},$$

where $\boldsymbol{\xi}_i$ is the i th discrete velocity and $c_s = 1/\sqrt{3}$ is the model speed of sound. To fulfill the relation of Eq. (3) at the discrete level, the equilibrium DF f^E in present research is evaluated by

$$f^E = \mathbf{M}^{-1} \mathbf{m}^E, \tag{4}$$

where $f^E = \{f_0^E, f_1^E, \dots, f_8^E\}^T$ represents the column vector constituted by the discrete equilibrium DFs, \mathbf{M} is the transformation matrix defined as

$$M = \begin{bmatrix} 1 & 1 & 1 & 1 & 1 & 1 & 1 & 1 & 1 \\ -4 & -1 & -1 & -1 & -1 & 2 & 2 & 2 & 2 \\ 4 & -2 & -2 & -2 & -2 & 1 & 1 & 1 & 1 \\ 0 & 1 & 0 & -1 & 0 & 1 & -1 & -1 & 1 \\ 0 & -2 & 0 & 2 & 0 & 1 & -1 & -1 & -1 \\ 0 & 0 & 1 & 0 & -1 & 1 & 1 & -1 & -1 \\ 0 & 0 & -2 & 0 & 2 & 1 & 1 & -1 & -1 \\ 0 & 1 & -1 & 1 & -1 & 0 & 0 & 0 & 0 \\ 0 & 0 & 0 & 0 & 0 & 1 & -1 & 1 & -1 \end{bmatrix},$$

and m^E signifies the macroscopic equilibria:

$$m^E = \rho \left\{ 1, 3|\mathbf{u}|^2 - 2, \alpha - 3|\mathbf{u}|^2, u_x, -u_x, u_y, -u_y, u_x^2 - u_y^2, u_x u_y \right\}^T.$$

Here α is a free parameter used to eliminate the nonisotropic effects of the scheme [26].

The relations between the conservative variables and the discrete DFs become

$$\rho = \sum_i f_i = \sum_i f_i^E, \rho \mathbf{u} = \sum_i \xi_i f_i = \sum_i \xi_i f_i^E. \tag{5}$$

With the discretization of velocity space, the discrete velocity Boltzmann-BGK equation takes the following form:

$$\frac{\partial f_i}{\partial t} + \xi_i \cdot \nabla_{\mathbf{x}} f_i = \Omega_i \equiv -\frac{f_i - f_i^E}{\tau}. \tag{6}$$

To numerically solve Eq. (6), we first subdivide the spatial domain into a set of grid cells and integrate this equation over a certain cell, which yields

$$\frac{d}{dt} \int_{V_c} f_i(\mathbf{x}, t) d\mathbf{x} + \int_{\partial V_c} (\xi \cdot \mathbf{n}) f_i(\mathbf{x}, t) dS = \int_{V_c} \Omega_i(\mathbf{x}, t) d\mathbf{x}, \tag{7}$$

where V_c represents the integral cell centered at position \mathbf{x}_c , ∂V_c indicates the surface bounding the cell, and \mathbf{n} represents the unit vector normal to the surface. Integrating Eq. (7) over a time step of length $\Delta t = t_{n+1} - t_n$ yields

$$f_i^{n+1} - f_i^n + \frac{\Delta t}{|V_c|} F_i^{n+1/2} = \frac{\Delta t}{2} [\Omega_i^{n+1} + \Omega_i^n], \tag{8}$$

where $|V_c|$ measures the volume of cell V_c , f_i^n and Ω_i^n approximate the cell averages of V_c in such a way that

$$f_i^n = \frac{1}{|V_c|} \int_{V_c} f_i(\mathbf{x}, t_n) d\mathbf{x}, \tag{9a}$$

$$\Omega_i^n = \frac{1}{|V_c|} \int_{V_c} \Omega_i(\mathbf{x}, t_n) d\mathbf{x}, \tag{9b}$$

$F_i^{n+1/2}$ measures the kinetic flux at the mid time $t_n + \Delta t/2$ by

$$F_i^{n+1/2} = \int_{\partial V_c} (\xi_i \cdot \mathbf{n}) f_i(\mathbf{x}, t_n + \Delta t/2) dS. \tag{10}$$

Note that the midpoint rule is utilized to compute the time integral of the kinetic flux and trapezoidal rule is employed to evaluate the time integral of the collision term in Eq. (8). To obtain a fully explicit evolution equation, two auxiliary distribution functions are introduced:

$$\tilde{f}_i = f_i - \frac{\Delta t}{2} \Omega_i, \tilde{f}_i^+ = f_i + \frac{\Delta t}{2} \Omega_i. \tag{11}$$

Substituting Eq. (11) into Eq. (8), we have

$$\tilde{f}_i^{n+1} = \tilde{f}_i^{+,n} - \frac{\Delta t}{|V_c|} F_i^{n+1/2}, \tag{12}$$

which turns out to be fully explicit.

To evaluate the kinetic flux $F_i^{n+1/2}$, the primitive distribution function $f_i(\mathbf{x}_f, t_{n+1/2})$ on cell interface is needed. To this end, we integrate Eq. (6) along the characteristic line over a time step length of $\delta t = \Delta t/2$:

$$f_i(\mathbf{x}_f, t_n + \delta t) - f_i(\mathbf{x}_f - \boldsymbol{\xi}_i \delta t, t_n) = \frac{\delta t}{2} [\Omega_i(\mathbf{x}_f, t_n + \delta t) + \Omega_i(\mathbf{x}_f - \boldsymbol{\xi}_i \delta t, t_n)]. \tag{13}$$

Here the trapezoidal rule is once again employed to evaluate the time integral of collision term. To realize the explicit treatment of Eq. (13), another two auxiliary distribution functions are introduced as follows:

$$\bar{f}_i = f_i - \frac{\delta t}{2} \Omega_i, \bar{f}_i^+ = f_i + \frac{\delta t}{2} \Omega_i. \tag{14}$$

Eq. (13) then can be rearranged as

$$\bar{f}_i(\mathbf{x}_f, t_n + \delta t) = \bar{f}_i^+(\mathbf{x}_f - \boldsymbol{\xi}_i \delta t, t_n). \tag{15}$$

The cell-centered auxiliary distribution function f_i^+ can be constructed according to its definition:

$$\bar{f}_i^+ = f_i + \frac{\delta t}{2} \Omega_i = \frac{2\tau - \delta t}{2\tau} f_i + \frac{\delta t}{2\tau} f_i^E. \tag{16}$$

The value of $f_i^+(\mathbf{x}_f - \boldsymbol{\xi}_i \delta t, t_n)$ can be interpolated from the corresponding cell-centered distribution function [53]. For the face-based reconstruction scheme (FRS), $f_i^+(\mathbf{x}_f - \boldsymbol{\xi}_i \delta t, t_n)$ can be evaluated by

$$f_i^+(\mathbf{x}_f - \boldsymbol{\xi}_i \delta t, t_n) = f_i^+(\mathbf{x}_f, t_n) - \boldsymbol{\xi}_i \delta t \cdot \nabla f_i^+(\mathbf{x}_f, t_n). \tag{17}$$

For the cell-based reconstruction scheme (CRS), $f_i^+(\mathbf{x}_f - \boldsymbol{\xi}_i \delta t, t_n)$ can be computed by

$$\bar{f}_i^+(\mathbf{x}_f - \boldsymbol{\xi}_i \delta t) = \begin{cases} \bar{f}_i^+(\mathbf{x}_L) + (\mathbf{x}_f - \mathbf{x}_L - \boldsymbol{\xi}_i \delta t) \cdot \nabla \bar{f}_i^+(\mathbf{x}_L) + \frac{1}{2} (\mathbf{x}_f - \mathbf{x}_L - \boldsymbol{\xi}_i \delta t)^2 \cdot \nabla^2 \bar{f}_i^+(\mathbf{x}_L), & \boldsymbol{\xi}_i \cdot \mathbf{n} \leq 0, \\ \bar{f}_i^+(\mathbf{x}_R) + (\mathbf{x}_f - \mathbf{x}_R - \boldsymbol{\xi}_i \delta t) \cdot \nabla \bar{f}_i^+(\mathbf{x}_R) + \frac{1}{2} (\mathbf{x}_f - \mathbf{x}_R - \boldsymbol{\xi}_i \delta t)^2 \cdot \nabla^2 \bar{f}_i^+(\mathbf{x}_R), & \boldsymbol{\xi}_i \cdot \mathbf{n} \geq 0, \end{cases} \tag{18}$$

where \mathbf{x}_L and \mathbf{x}_R correspond respectively to the center positions of the two cells adjacent to the interface located at \mathbf{x}_f . Once the value of f_i^+ is known, the primitive DF at cell interface can be updated by

$$f = \frac{2\tau}{2\tau + \delta t} \bar{f} + \frac{\delta t}{2\tau + \delta t} f^E. \tag{19}$$

Thereafter the kinetic flux $F^{n+1/2}$ can be evaluated according to Eq. (10) and the auxiliary distribution function at time t_{n+1} can be updated via Eq. (12). The cell-averaged primitive DF then can be obtained according to

$$f = \frac{2\tau}{2\tau + \Delta t} \tilde{f} + \frac{\Delta t}{2\tau + \Delta t} f^E. \tag{20}$$

To obtain the primitive DFs in Eq. (19) and (20), the value of equilibrium DFs that depend on the conservative variables should be first determined via Eq. (4). With the help of Eq. (5), the corresponding conservative variables can be evaluated by

$$\rho = \sum_i f_i = \sum_i \bar{f}_i, \rho \mathbf{u} = \sum_i \xi_i f_i = \sum_i \xi_i \bar{f}_i \tag{21}$$

on cell interfaces and by

$$\rho = \sum_i f_i = \sum_i \tilde{f}_i, \rho \mathbf{u} = \sum_i \xi_i f_i = \sum_i \xi_i \tilde{f}_i \tag{22}$$

at cell centers.

To date, the evolution process of DUGKS without considering force effects has been basically explained. To incorporate the influence of external forces, another discrete distribution function f_i^S accounting for the force effects should be introduced:

$$\frac{\partial f_i}{\partial t} + \xi_i \cdot \nabla_x f_i = \Omega_i \equiv -\frac{f_i - f_i^E}{\tau} + f_i^S. \tag{23}$$

To correctly recover the macroscopic equations, the moments of discrete force DF should obey

$$\sum_i f_i^S = 0, \sum_i \xi_i f_i^S = \mathbf{F}, \sum_i \xi_i \xi_i f_i^S = \mathbf{u}\mathbf{F} + \mathbf{F}\mathbf{u}, \tag{24}$$

where $\mathbf{F} = \mathbf{F}_s + \mathbf{G}$ is the external force in total. In present research the force DF f^S is evaluated by

$$f^S = \mathbf{M}^{-1} \mathbf{m}^S, \tag{25}$$

where $f^S = \{f_0^S, f_1^S, \dots, f_8^S\}$ represents the column vector constituted by the discrete force DFs, \mathbf{M} is the identical transformation matrix appeared in Eq. (4), and \mathbf{m}^S signifies the macroscopic force terms expressed as

$$\mathbf{m}^S = \{0, 6\mathbf{u} \cdot \mathbf{F}, -6\mathbf{u} \cdot \mathbf{F}, F_x, -F_x, F_y, -F_y, 2(F_x u_x - F_y u_y), F_x u_y + F_y u_x\}.$$

To circumvent the force effects on the interface flux, the Strang-splitting scheme is employed to evaluate the force influences. With such a treatment, the force effects are incorporated before and after the DUGKS procedure in a way that

$$\frac{\partial f_i}{\partial t} = \frac{1}{2} f_i^S, \tag{26a}$$

$$\frac{\partial f_i}{\partial t} + \xi_i \cdot \nabla_{\mathbf{x}} f_i = \Omega_i \equiv -\frac{f_i - f_i^E}{\tau}, \tag{26b}$$

$$\frac{\partial f_i}{\partial t} = \frac{1}{2} f_i^S. \tag{26c}$$

As Eq. (26b) remains identical to Eq. (6), it can be solved by the DUGKS procedure addressed previously. Eq. (26a) and (26c) can be numerically solved by the Euler forward method:

$$f_i^* = f_i^n + \frac{\Delta t}{2} f_i^{S,n}. \tag{27}$$

The conservative variables should be accordingly updated via

$$\rho^* = \rho^n, \mathbf{u}^* = \mathbf{u}^n + \frac{\Delta t}{2} \frac{\mathbf{F}^n}{\rho^n}. \tag{28}$$

2.3 Pseudopotential multiphase model

In the pseudopotential multiphase model, the interaction effects between/among different phases are mimicked by a volumetric force defined as

$$\mathbf{F}_s = -G\psi(\mathbf{x}) \sum_{i=1}^N \omega(|\mathbf{x}'_i - \mathbf{x}|^2) \psi(\mathbf{x}'_i) (\mathbf{x}'_i - \mathbf{x}), \tag{29}$$

where ψ represents the interaction potential, G indicates the interaction strength, ω stands for the weights, \mathbf{x}'_i denotes the nearby position that is related to \mathbf{x} by $\mathbf{x}'_i = \mathbf{x} + \xi_i \delta'_t$, among which ξ_i is the i th discrete velocity and δ'_t is the transporting time. A utilization of nine discrete velocity points leads to the following relation:

$$\omega(1) = 1/3, \omega(2) = 1/12, N = 8, \delta'_t = 1. \tag{30}$$

In fact, the role of expression $\sum_{i=1}^N \omega(|\mathbf{x}'_i - \mathbf{x}|^2) \psi(\mathbf{x}'_i) (\mathbf{x}'_i - \mathbf{x})$ in Eq. (29) is equivalent to evaluating the gradient of ψ through an isotropic finite-difference scheme [54]. A Taylor expansion of Eq. (29) gives

$$\mathbf{F}_s = -G\delta_x^2 \left[\psi \nabla \psi + \frac{\delta_x^2}{6} \nabla \left(\nabla^2 \psi \right) \right] + O(\nabla^5), \tag{31}$$

where $\delta_x = \xi_x \delta'_t = \xi_y \delta'_t = 1$ measures the grid spacing. To analytically derive the pressure tensor, Eq. (31) could be reformulated as [20]

$$\mathbf{F}_s = -\frac{G\delta_x^2}{2} \nabla \cdot (\psi^2 \mathbf{I}) - \frac{G\delta_x^4}{6} \nabla \cdot \left[\left(\psi \nabla \cdot \nabla \psi + \frac{1}{2} \nabla \psi \cdot \nabla \psi \right) \mathbf{I} - \nabla \psi \nabla \psi \right] + O(\nabla^5), \tag{32}$$

where \mathbf{I} represents the identity matrix. However, Sbragaglia *et al.* [21] demonstrate that the transformation of Eq. (31) into Eq. (32) does not necessarily guarantee uniqueness. As a matter of fact, Eq. (31) can be reformulated as

$$\begin{aligned} \mathbf{F}_s = & -\frac{G\delta_x^2}{2} \nabla \cdot (\psi^2 \mathbf{I}) - \frac{G\delta_x^4}{6} \nabla \cdot (a_1 \nabla \psi \nabla \psi + a_2 \psi \nabla \nabla \psi) \\ & - \frac{G\delta_x^4}{6} \nabla \cdot (a_3 \nabla \psi \cdot \nabla \psi + a_4 \psi \nabla \cdot \nabla \psi) \mathbf{I} + O(\nabla^5), \end{aligned} \tag{33}$$

providing the prefactors satisfy

$$\begin{cases} a_1 + a_2 + 2a_3 = 0, \\ a_1 + a_4 = 0, \\ a_2 + a_4 = 1. \end{cases} \tag{34}$$

It can be identified that Eq. (32) represents a special case of Eq. (33) at $a_1 = -1, a_2 = 0, a_3 = 1/2, a_4 = 1$.

The continuum pressure tensor is defined as [26]

$$\nabla \cdot \mathbf{P} = \nabla (\rho c_s^2) - \mathbf{F}_s - \mathbf{S}, \tag{35}$$

where c_s stands for the model speed of sound and \mathbf{S} represents the additional term introduced from the discretization of DUGKS. Due to the reconstruction approaches utilized, the additional term \mathbf{S} contributed from DUGKS lacks of isotropy. To balance the anisotropic influences, a free parameter α has been introduced in Eq. (4). As the discretization approaches utilized in DUGKS appear to be complex, it is quite difficult to obtain the general expression of \mathbf{P} . Nevertheless, the normal pressure P_n in such a condition could be similarly postulated as [55]

$$P_n = \rho RT + \frac{G\delta_x^2}{2} \psi^2 + \frac{G\delta_x^4}{12} \left[-k_1 \left(\frac{d\psi}{dx} \right)^2 + 2k_2 \psi \frac{d^2\psi}{dx^2} \right], \tag{36}$$

where n denotes the direction normal to the interface. The normal component of the pressure tensor P_n at the equilibrium state should be equal to the bulk pressure p_0 [22]. The mechanical stability condition can then be obtained as [8]

$$\int_{\rho_g}^{\rho_l} (p_0 - p_{\text{EOS}}) \frac{\psi'}{\psi^{1+\epsilon}} d\rho = 0, \tag{37}$$

where $\psi' = d\psi/d\rho$, $\epsilon = k_1/k_2$, $p_0 = p(\rho_l) = p(\rho_g)$ denotes the bulk pressure and p_{EOS} represents the non-ideal equation of state (EOS) in terms of the pseudopotential model:

$$p_{\text{EOS}} = \rho c_s^2 + \frac{G\delta_x^2}{2} \psi^2. \tag{38}$$

Providing the coexistence densities (ρ_l and ρ_g) have been estimated by DUGKS, the value of the produced parameter ϵ can then be determined numerically [25]. To consider the effects of various non-ideal equations of state, He and Doolen [19] pointed out that the pseudopotential ψ should be evaluated as

$$\psi = \sqrt{\frac{2(p_{\text{EOS}} - \rho c_s^2)}{G\delta_x^2}}, \tag{39}$$

where p_{EOS} should be one of the non-ideal equations of state in the thermodynamic theory. In present research, the dimensionless van der Waals equation of state (vdW-EOS) expressed as

$$p_{\text{EOS}} = \frac{\rho T}{1 - b\rho} - a\rho^2 \tag{40}$$

is employed, with $a = 9/392$ and $b = 2/21$. The critical density ρ_c and temperature T_c hold the value of $7/2$ and $1/14$ in such a condition [56]. With the incorporation of the dimensionless vdW-EOS, the pseudopotential ψ could be directly calculated through Eq. (39).

3 Numerical tests

The capacity of pseudopotential-based DUGKS is validated by three benchmark tests. Firstly, the fundamental capability to predict coexistence densities is verified by the flat interface test. Subsequently, the nonisotropic property is investigated by the quiescent droplet test and the isotropy-preserving parameter α is tuned to cancel out the nonisotropic effects. Finally, the spinodal decomposition test is conducted to examine its isotropy-preserving property in transient conditions. For steady tests, the computing process terminates when the L_2 -norm-based velocity error $E(\mathbf{u})$ falls below a critical value e :

$$E(\mathbf{u}) = \sqrt{\frac{\sum_{\mathbf{x}} |\mathbf{u}(\mathbf{x}, t_n) - \mathbf{u}(\mathbf{x}, t_{n-1000})|^2}{\sum_{\mathbf{x}} |\mathbf{u}(\mathbf{x}, t_n)|^2}} < e, \tag{41}$$

where \mathbf{u} denotes the velocity field, t_{n-1000} indicates the moment 1000 time steps ahead of t_n and e is given as 10^{-8} if not otherwise specified. The CFL number is fixed at 0.8 across all the tests.

3.1 Flat interface

The flat interface problem serves as a fundamental benchmark for validating the basic capability of newly proposed multiphase models. Consider an infinitely long horizontal channel filled with binary fluids of different phases. The liquid resides in the middle half of the channel while the gas occupies the upper and bottom region. The computational domain is confined to a 16×256 rectangular region uniformly divided into Cartesian grids, where the grid spacing holds a fixed value of unity. Periodical boundary conditions are applied to all sides. The density field is initialized by

$$\rho(x, y) = \rho_g + \frac{\rho_l - \rho_g}{2} \left[\tanh \frac{2(y - y_L)}{W} - \tanh \frac{2(y - y_H)}{W} \right], \tag{42}$$

where ρ_l and ρ_g correspond to the liquid and gas densities, y_L and y_H represent the lower and upper bound of the fluid in liquid phase, and W denotes the interface thickness. Figure 1 presents the coexisting densities produced respectively by DUGKS and LBM at $\tau =$

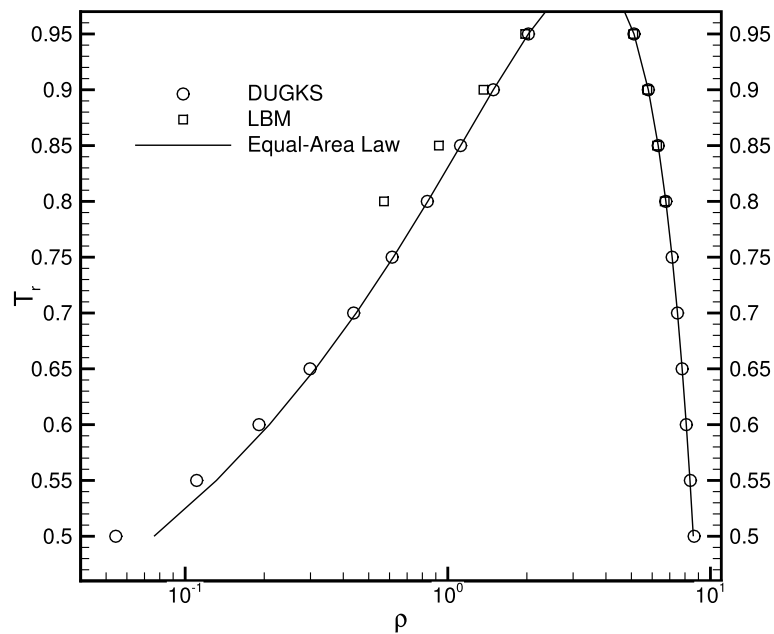


Fig. 1 Coexisting curves produced by DUGKS and LBM, $\tau = 0.3, \alpha = 1.0$

0.3, $\alpha = 1.0$. It can be identified that the results provided by DUGKS agree well with the theoretical solutions obtained through the Maxwell equal-area law [27] while the results offered by LBM deviate significantly from the theoretical solutions. Moreover, DUGKS operates properly in conditions of low temperatures whereas LBM fails to work when $T_r < 0.75$. The inferior results produced by the standard LBM could be attributed to the superfluous terms recovered in the momentum equation [56]. The stability superiority of DUGKS might result from the coupling of transport and collision process. The influences of isotropy-preserving parameter α on the coexisting densities are investigated and the corresponding results are presented in Fig. 2. Numerical results remain unchanged despite the varying parameter α . As the density distributions in the horizontal direction stay unaltered, which has no impact on the fluid behavior, it is reasonable to obtain identical results with varying α . The density profiles along the vertical direction produced by DUGKS at different temperatures are illustrated in Fig. 3. With the increasing temperature, the flat interface gets sharpened, which is due to the strong coupling of physical properties originating from the pseudopotential model [27]. The varying interface thickness also suggests that W in Eq. (42) has no concrete meaning and remains useful only during the initialization process.

3.2 Quiescent droplet

The quiescent droplet provides another fundamental benchmark for validating the model’s capability. With this test, we specially investigated the isotropic property of pseudopotential-based DUGKS. Initially, a circular droplet is placed at the center of a $L_0 \times L_0$ square domain according to

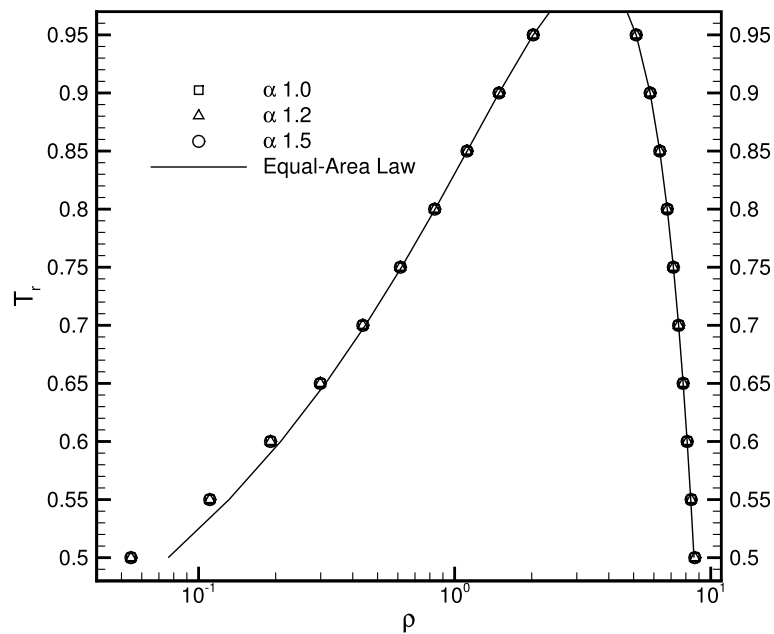


Fig. 2 Coexisting curves produced by DUGKS with varying values of isotropy-preserving parameter α , $\tau = 0.3$

$$\rho(x, y) = \frac{\rho_l + \rho_g}{2} - \frac{\rho_l - \rho_g}{2} \tanh \left[\frac{2 \left(\sqrt{|x - x_c|^2 + |y - y_c|^2} - R_d \right)}{W} \right], \quad (43)$$

where ρ_l and ρ_g correspond respectively to the liquid and gas density, (x_c, y_c) represents the center position of the square domain, and R_d denotes the droplet radius. The parameters in this test are set as $L_0 = 256$, $R_d = 0.24L_0$, $W = 5$. The computing process terminates once the L_2 -norm-based velocity error meets the relation defined by Eq. (41). Figure 4 shows the density distribution at the initial moment. The ultimate density contours produced by DUGKS using different reconstruction schemes are illustrated in Fig. 5. The square droplet presented in Fig. 5a is obtained with the second-order face-based reconstruction scheme, i.e., the central-difference scheme [28]. The nearly circular droplet shown in Fig. 5b is produced by the second-order cell-based reconstruction scheme, also known as the upwind scheme [57]. As a matter of fact, it is Dr. Wang Peng [51] who first identified the nonisotropic property of the pseudopotential-based DUGKS. In the spring of 2018, Wang and Zhu [57] dropped in at NWPU and gave a brief presentation themed around DUGKS. During a casual conversation, we talked about the nonisotropic property of the pseudopotential-based DUGKS. Wang suggests that the upwind reconstruction approach, together with the Strang-splitting scheme, should be employed to obtain an isotropic interface. Following this idea, we conducted a few simulations with the pseudopotential-based DUGKS. It turned out that although the nonisotropic problem could be relieved to some extent, the pseudopotential-based DUGKS still fails to produce a perfectly isotropic interface, which has been demonstrated by the interface profile presented in Fig. 5b. The droplet produced with a third-order accuracy of CRS is illustrated in Fig. 5c. It can be observed that employing a high-order upwind

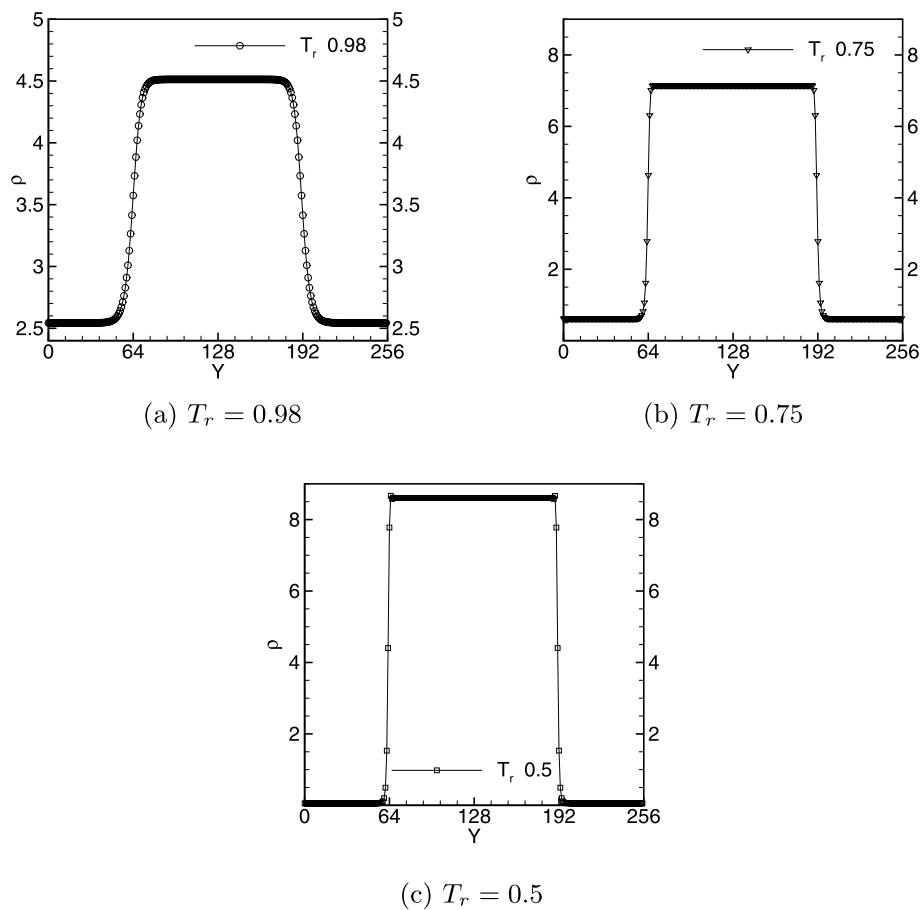


Fig. 3 Density profile produced by DUGKS with varying temperatures, $\tau = 0.3$

reconstruction scheme contributes little to the elimination of nonisotropic deficiency. Through a third-order Chapman-Enskog analysis, Huang *et al.* [26] identified the non-isotropic and isotropic terms in the pseudopotential model. Numerical results proved that the free parameter α played a key role in preserving the isotropic property. With this proof, we introduced the isotropy-preserving parameter α in the calculation of the equilibrium distribution function. By adjusting α to an appropriate value, a perfectly isotropic interface can be produced and maintained. In the condition of $\tau = 0.3$, $T_r = 0.95$, the corresponding value of α is 1.304. The circular droplet produced is illustrated in Fig. 5d. In practical computations, the density criterion and the velocity criterion have been compared to identify the optimal criterion for the determination of α . The density criterion compares the final density field with the initial density field and recognizes the value of α that creates the minimum density difference as the most appropriate choice. The velocity criterion considers the value of α that generates the minimum L_2 norm of velocity as the most appropriate choice. An optimal criterion should help maintain the quiescent interface as isotropic as possible. The isotropic level of an interface is assessed by comparing the horizontal density profile with the diagonal density profile produced at a final moment. Through a series of comparisons, it has been identified that the velocity criterion best determines the value of α . Figure 6 illustrates the density contour

produced by DUGKS on different criteria. It can be observed that the interface generated under the density criterion suffers from a nonisotropic problem while the interface created under the velocity criterion maintains excellent isotropy. Numerical experiments also revealed that the appropriate value of α varies along with changes in the relaxation time τ or the reduced temperature T_r . Through repeated calibration, we ascertained the specific values of α for preserving an isotropic interface. Figure 7 illustrates the ternary relation diagram for α , τ and T_r . Table 1 presents the detailed data. With this information, it is now possible to interpolate the specific value of α for a wide range of T_r and τ . Considering the situation of $\tau = 0.63$ and $T_r = 0.72$, the most appropriate value of α determined by numerical simulations is 1.025 while the interpolated value of α in such a condition is 1.02494, which is pretty close to the calibrated value. Figure 8 compares the density profiles extracted from various directions. The density profile along the horizontal direction coincides completely with the profile along the vertical direction. The profile along the diagonal direction deviates slightly from them, which could be partially attributed to the additional error introduced during data extraction. Nevertheless, the nearly indistinguishable deviation demonstrates the well-maintained isotropic property of the interface. It is worth mentioning that we failed to find an analytical expression to describe the mapping relation between τ , T_r , and α , which might be beneficial for the application of pseudopotential-based DUGKS.

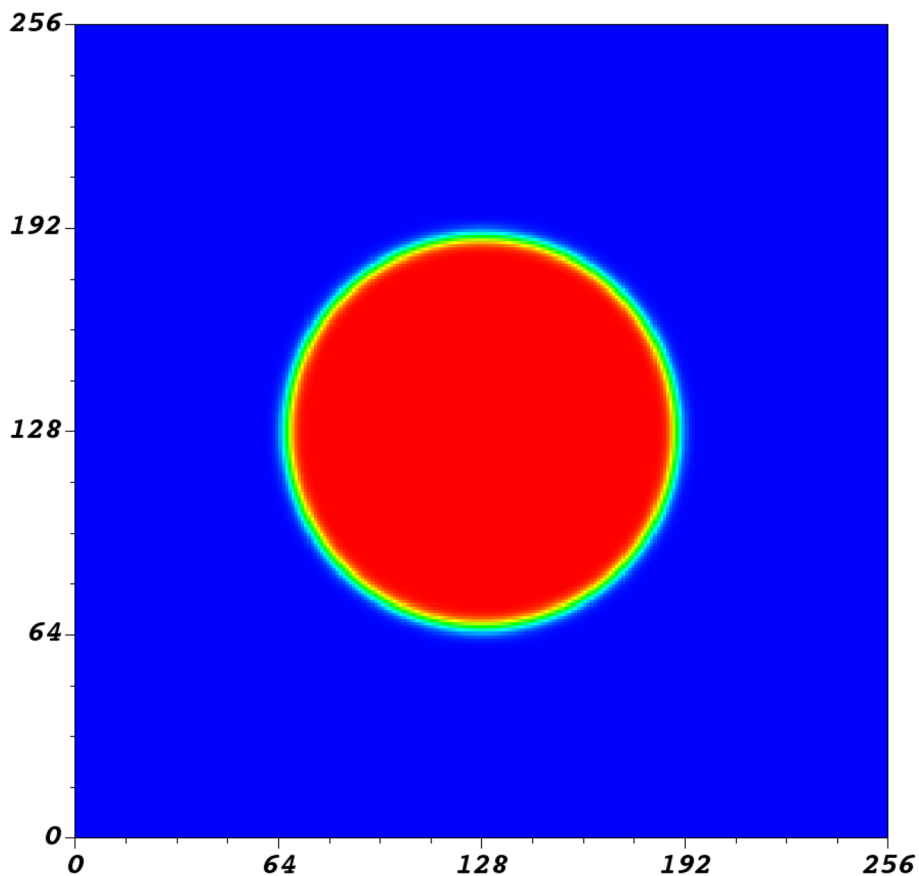


Fig. 4 Distribution of density field at initial moment, $\tau = 0.3, T_r = 0.95$

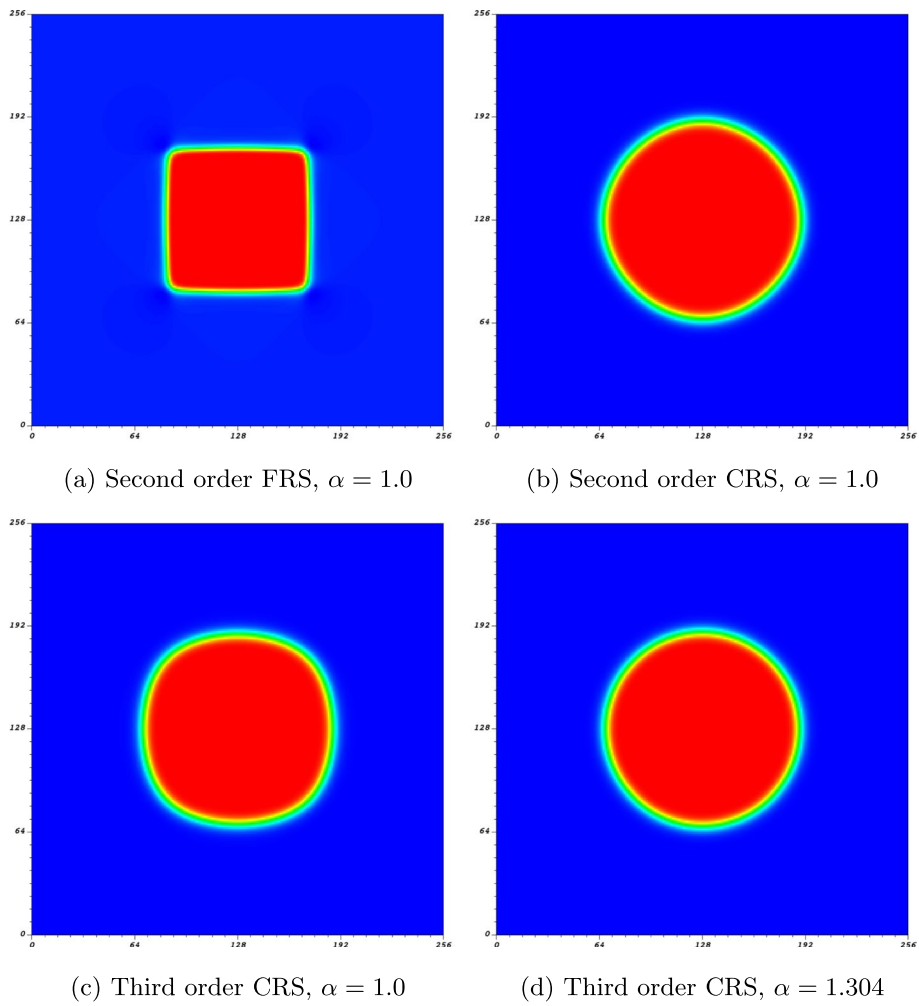


Fig. 5 Density contours produced by DUGKS employing different reconstruction schemes, $\tau = 0.3, T_r = 0.95$

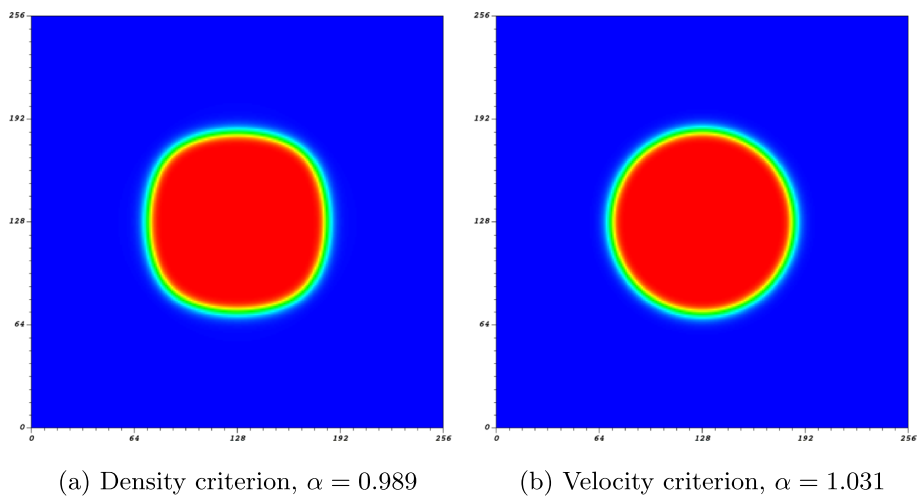


Fig. 6 Density contours produced by DUGKS on different criteria, $\tau = 0.75, T_r = 0.95$

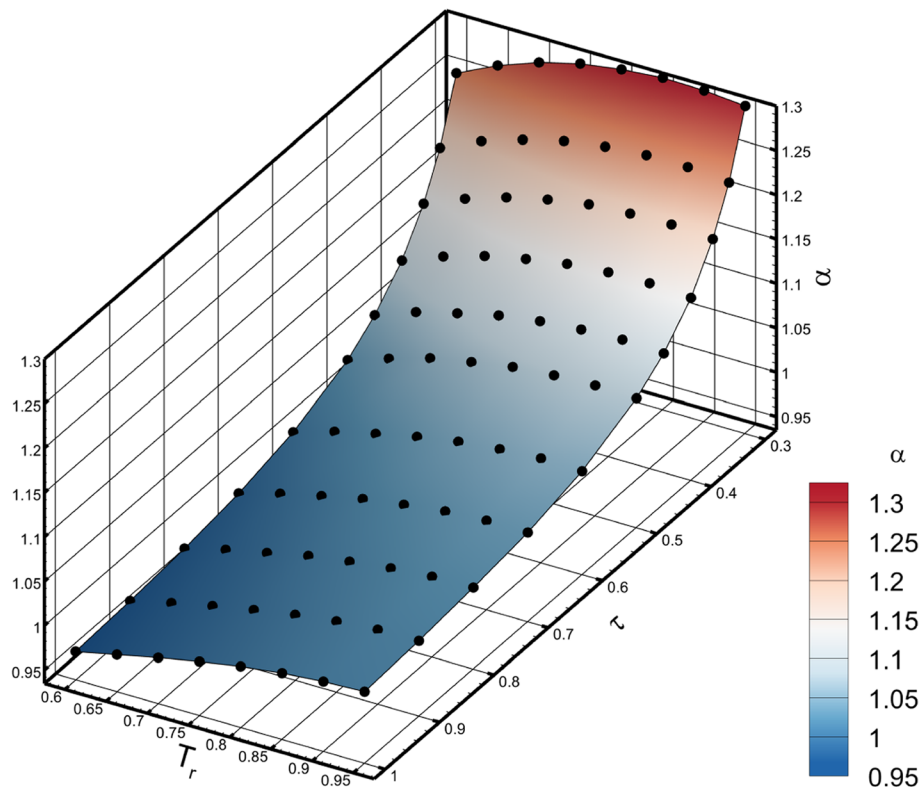


Fig. 7 Variation of isotropy-preserving parameter α with regard to relaxation time τ and reduced temperature T_r

Table 1 Variation of isotropy-preserving parameter α with regard to relaxation time τ and reduced temperature T_r

| τ | 0.3 | 0.33 | 0.36 | 0.4 | 0.45 | 0.5 | 0.6 | 0.7 | 0.8 | 0.9 | 1.0 |
|------------|-------|-------|-------|-------|-------|-------|-------|-------|-------|-------|-------|
| $T_r 0.95$ | 1.304 | 1.234 | 1.186 | 1.141 | 1.105 | 1.081 | 1.052 | 1.036 | 1.027 | 1.02 | 1.016 |
| $T_r 0.9$ | 1.308 | 1.238 | 1.189 | 1.144 | 1.107 | 1.082 | 1.053 | 1.036 | 1.026 | 1.019 | 1.014 |
| $T_r 0.85$ | 1.309 | 1.238 | 1.188 | 1.143 | 1.105 | 1.08 | 1.05 | 1.033 | 1.022 | 1.015 | 1.01 |
| $T_r 0.8$ | 1.305 | 1.234 | 1.185 | 1.139 | 1.101 | 1.076 | 1.045 | 1.027 | 1.016 | 1.009 | 1.004 |
| $T_r 0.75$ | 1.298 | 1.227 | 1.177 | 1.131 | 1.094 | 1.068 | 1.037 | 1.020 | 1.009 | 1.001 | 0.996 |
| $T_r 0.7$ | 1.286 | 1.215 | 1.166 | 1.121 | 1.083 | 1.059 | 1.027 | 1.010 | 0.999 | 0.992 | 0.987 |
| $T_r 0.65$ | 1.269 | 1.200 | 1.151 | 1.107 | 1.071 | 1.045 | 1.016 | 0.999 | 0.989 | 0.982 | 0.977 |
| $T_r 0.6$ | 1.247 | 1.179 | 1.132 | 1.089 | 1.054 | 1.030 | 1.002 | 0.986 | 0.977 | 0.971 | 0.967 |

To quantitatively examine the accuracy of the current scheme, we further validated the Laplace’s law by simulating a number of quiescent droplets with varying radii. Figure 9 illustrates the relation between the pressure jump ΔP and the reciprocal of radius. Obvious linear relation could be identified from the results produced by DUGKS with different temperatures, which is in accordance with the Laplace’s law: $\Delta P = \sigma/R_d$. Due to the strong coupling effects of the pseudopotential model, it is generally difficult to determine the theoretical value of surface tension coefficient

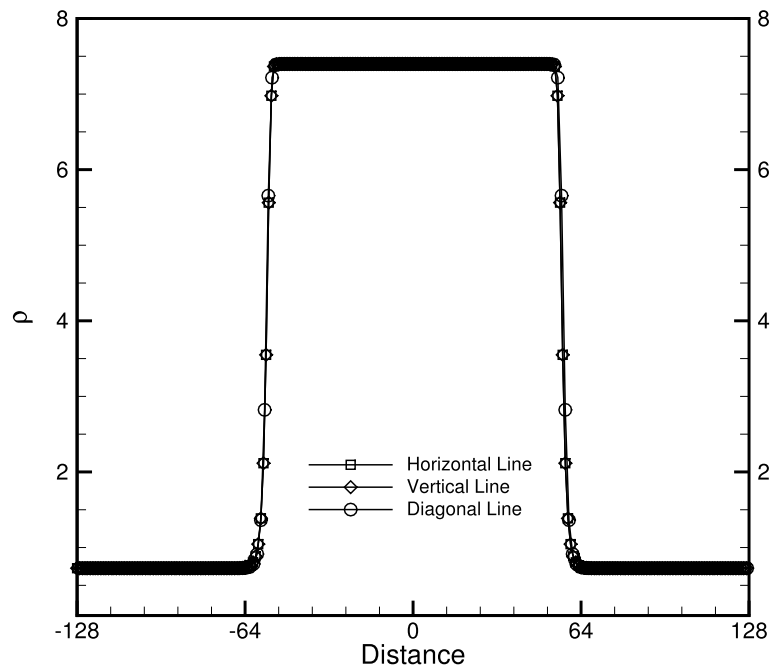


Fig. 8 Density profiles along horizontal direction ($Y = 128$), vertical direction ($X = 128$), and diagonal direction, $\tau = 0.63, T_r = 0.72, \alpha = 1.025$

σ . For the same reason, the droplet radius obtained at the final moment could deviate slightly from the initialization value. Nevertheless, the linear relation reflected by the numerical results could surely demonstrate the fundamental capability of pseudopotential-based DUGKS.

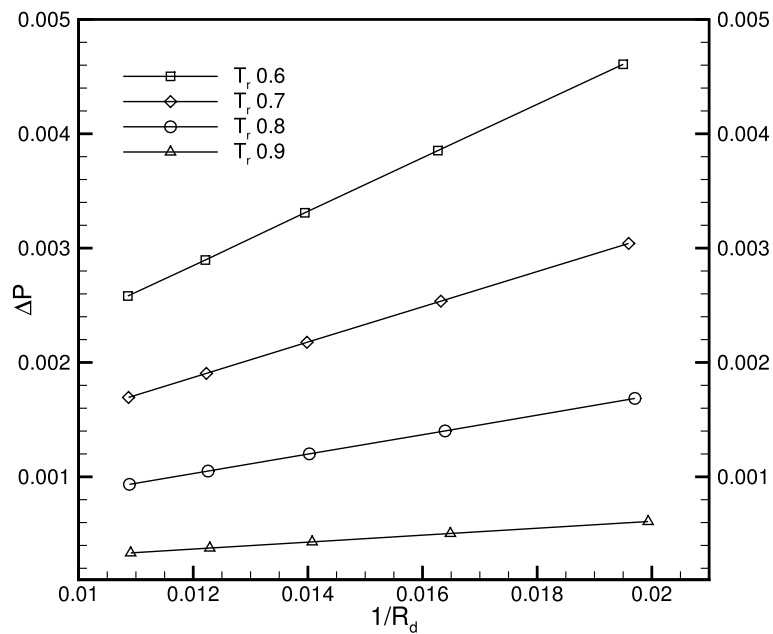
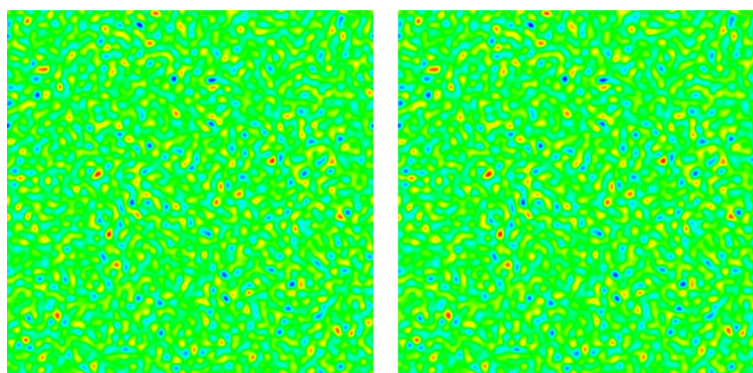
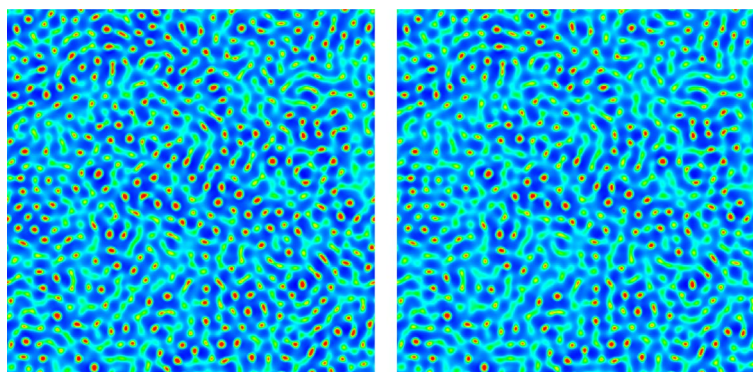


Fig. 9 Validation of Laplace's law, $\tau = 0.3$



(a) $\alpha = 1.305$ (b) $\alpha = 1.0$

Fig. 10 Snapshots of the spinodal decomposition process, $\tau = 0.3, T_r = 0.8, t = 80$



(a) $\alpha = 1.305$ (b) $\alpha = 1.0$

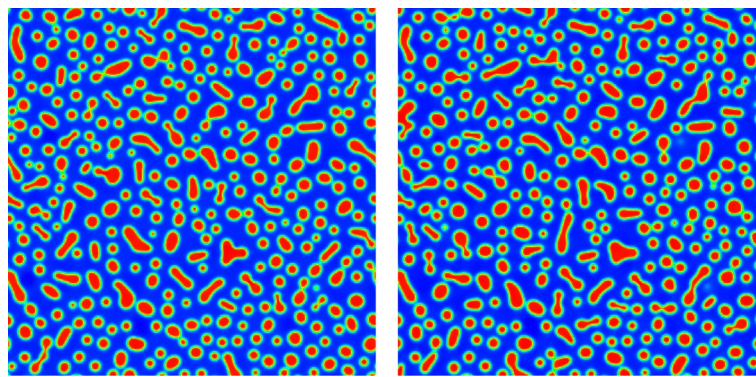
Fig. 11 Snapshots of the spinodal decomposition process, $\tau = 0.3, T_r = 0.8, t = 400$

3.3 Spinodal decomposition

The previous two benchmark tests belong to steady-state problems. To examine the capacity of DUGKS in dealing with transient problems, spinodal decomposition tests are conducted. Spinodal decomposition, also referred to as phase separation, occurs when a homogeneous mixture contains compositional fluctuations. The computational region is a $L_0 \times L_0$ square domain, with the side length L_0 set to 512. The relaxation time τ is fixed at 0.3 and the reduced temperature T_r is given as 0.8. The density field is initialized according to

$$\rho(x, y) = (\rho_l + \rho_g)/3 + \text{random}(0, 1)/100, \tag{44}$$

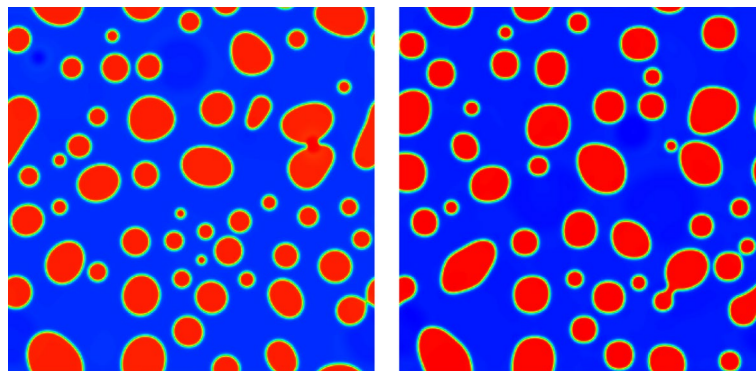
where $\text{random}(0, 1)$ generates the fluctuations by returning a random number between 0 and 1. Usually the evolution time should be scaled by a reference time relating to the surface tension coefficient σ . Due to the strong coupling effects of the pseudopotential model, it is difficult to determine the reference time. Here the simulation time t is directly used to indicate the time evolution. Figures 10, 11, 12, 13, 14, 15, 16, 17, 18 and 19 illustrate the comparative snapshots of the phase separation process produced by



(a) $\alpha = 1.305$

(b) $\alpha = 1.0$

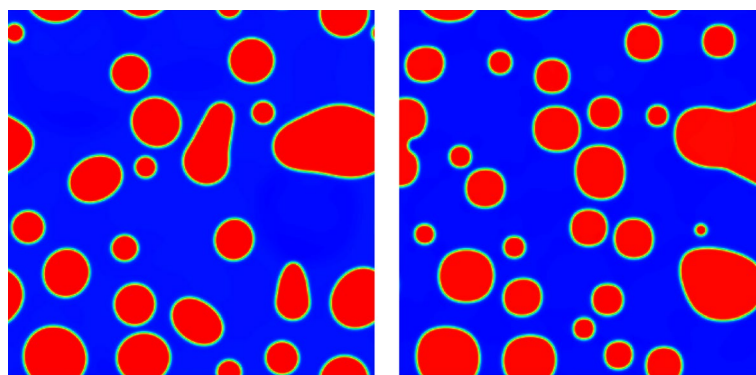
Fig. 12 Snapshots of the spinodal decomposition process, $\tau = 0.3, T_r = 0.8, t = 800$



(a) $\alpha = 1.305$

(b) $\alpha = 1.0$

Fig. 13 Snapshots of the spinodal decomposition process, $\tau = 0.3, T_r = 0.8, t = 4000$



(a) $\alpha = 1.305$

(b) $\alpha = 1.0$

Fig. 14 Snapshots of the spinodal decomposition process, $\tau = 0.3, T_r = 0.8, t = 8000$

DUGKS at $\tau = 0.3, T_r = 0.8$. The complete separation process is successfully predicted and no instability phenomenon has ever been detected. In the early stages depicted by Fig. 10, the tiny fluctuations evolve into local inhomogeneities that initialize the phase

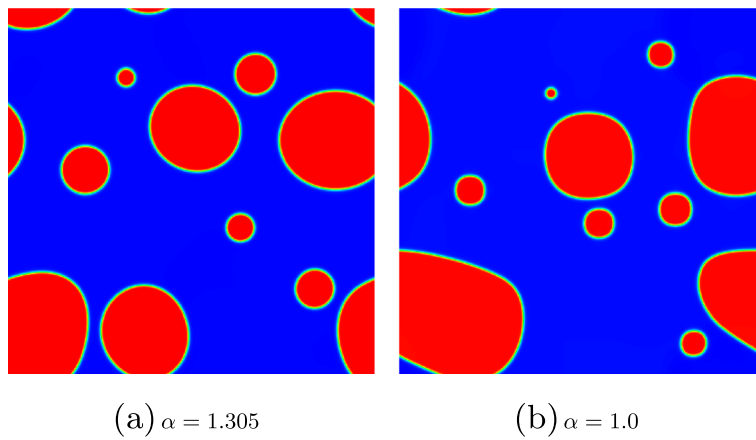


Fig. 15 Snapshots of the spinodal decomposition process, $\tau = 0.3, T_r = 0.8, t = 20000$

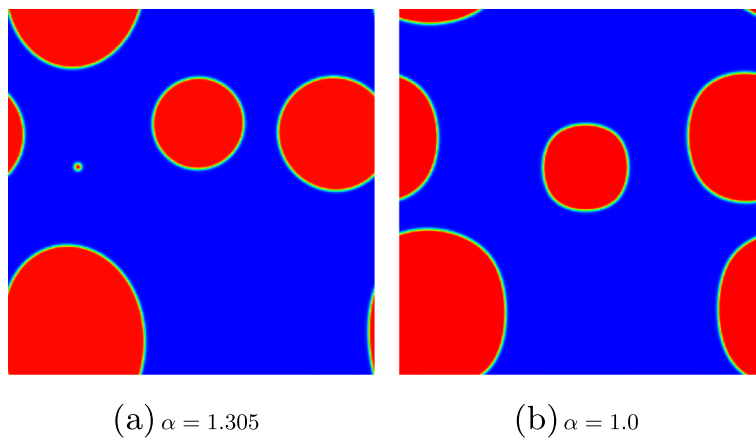


Fig. 16 Snapshots of the spinodal decomposition process, $\tau = 0.3, T_r = 0.8, t = 40000$

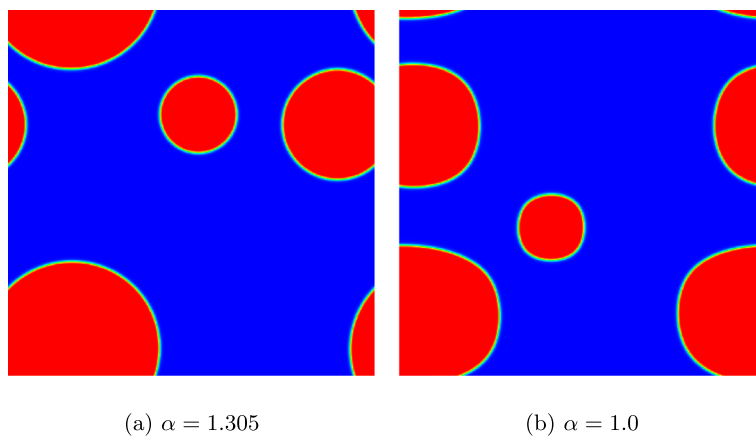


Fig. 17 Snapshots of the spinodal decomposition process, $\tau = 0.3, T_r = 0.8, t = 80000$

separation. As the system evolves, the inhomogeneities induce the nucleation of heavy liquid, which can be observed in Fig. 11. With the continual development, interfaces separating different phases can be clearly detected in Fig. 12. Then the small droplets

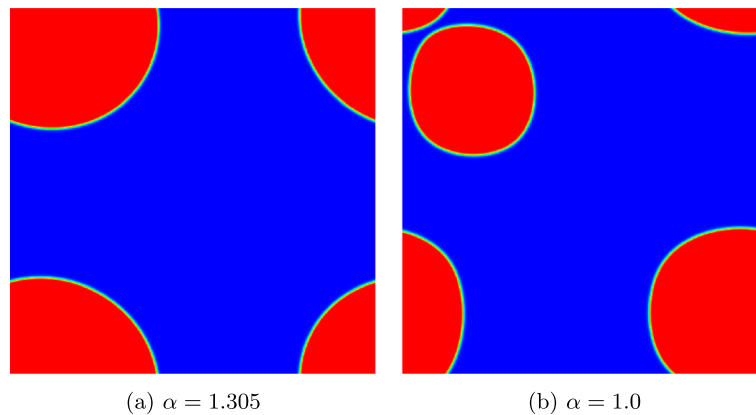


Fig. 18 Snapshots of the spinodal decomposition process, $\tau = 0.3, T_r = 0.8, t = 200000$

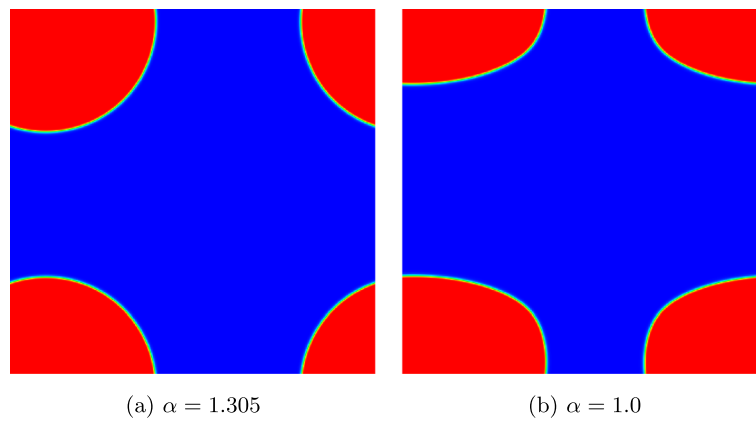


Fig. 19 Snapshots of the spinodal decomposition process, $\tau = 0.3, T_r = 0.8, t = 400000$

keep coalescing into large droplets. Eventually, a single quiescent droplet illustrated in Fig. 19 is formed. At the final moment, the interface produced with $\alpha = 1.035$ appears to be isotropic while the interface produced with $\alpha = 1.0$ suffers from a lack of isotropy. The same phenomenon can also be detected in the process of droplet coalescence depicted by Figs. 14, 15, 16, 17 and 18. This fact demonstrates the effectiveness of the isotropy-preserving property in a transient condition. The separation process produced with $\alpha = 1.0$ deviates slightly from the corresponding process built with $\alpha = 1.305$, which could be partially attributed to the differences in initial fluctuations.

4 Conclusion

A pseudopotential-based discrete unified gas-kinetic scheme for multiphase fluid flows is proposed by coupling the pseudopotential model into the Strang-splitting DUGKS. Due to the strict requirements of the scheme isotropy by the pseudopotential model, a direct coupling of pseudopotential model into DUGKS could not maintain an isotropic interface. To cancel out the nonisotropic terms introduced during the flux reconstruction process, the equilibrium distribution functions are expressed in a moment-based form and an isotropy-preserving parameter α is introduced. By adjusting this parameter

to the appropriate value, pseudopotential-based DUGKS managed to produce and maintain an isotropic interface. With a sequence of numerical experiments, we calibrate the value of α to facilitate DUGKS simulating isotropic interfaces in a wide range of conditions. Results produced in the spinodal decomposition tests further demonstrate the effectiveness of its isotropy-preserving property in the transient state. Comparative results of coexistence curves also proved the superior stability of DUGKS over that of LBM. The fundamental capacity of pseudopotential-based DUGKS has been demonstrated by the basic benchmark tests. Further investigations are needed to explore its capacity in specific fields.

5 Appendix

5.1 The nonisotropic property of DUGKS

The nonisotropic property caused by the kinetic flux reconstruction of DUGKS is explained. The discretized Boltzmann-BGK equation actually solved via DUGKS reads

$$\tilde{f}_i^{n+1} = \tilde{f}_i^{+,n} - \frac{\Delta t}{|V_c|} \sum_l^N (\boldsymbol{\xi}_i \cdot \mathbf{n}_l) f_i^{n+1/2} \Delta S_l, \tag{45}$$

where $|V_c|$ measures the volume of cell V_c centered at \mathbf{x}_c , N indicates the total number of surface elements bounding cell V_c , ΔS_l represents the area of l th surface element and \mathbf{n}_l denotes the unit vector normal to the surface element ΔS_l . The auxiliary distribution function \tilde{f}^+ could be expanded as

$$\tilde{f}_i^{+,n} = \tilde{f}_i^n - \frac{2\Delta t}{2\tau + \Delta t} (\tilde{f}_i^n - f_i^{E,n}), \tag{46}$$

which denotes a conservative collision process. The primitive distribution function $f^{n+1/2}$ on cell surface is evaluated via Eq. (19), which can be reformulated as the following collision process:

$$f_i^{n+1/2} = \bar{f}_i^{n+1/2} - \frac{\delta t}{2\tau + \delta t} (\bar{f}_i^{n+1/2} - f_i^{E,n+1/2}). \tag{47}$$

With this information, the flux term in Eq. (45) could be expanded as

$$\tilde{f}_i^{n+1} = \tilde{f}_i^{+,n} - \frac{\Delta t}{|V_c|} \sum_l^N (\boldsymbol{\xi}_i \cdot \mathbf{n}_l) \left[\bar{f}_i^{n+1/2} - \frac{\delta t}{2\tau + \delta t} (\bar{f}_i^{n+1/2} - f_i^{E,n+1/2}) \right] \Delta S_l. \tag{48}$$

Multiplying Eq. (48) by $\boldsymbol{\xi}_i$ and taking summation over i , we can obtain the following discrete momentum equation:

$$[\rho_c \mathbf{u}_c]^{n+1} = [\rho_c \mathbf{u}_c]^n - \frac{\Delta t}{|V_c|} \sum_l^N \left[\rho_l \mathbf{u}_l \mathbf{u}_l \cdot \mathbf{n}_l + c_s^2 \rho_l \mathbf{n}_l - \boldsymbol{\pi}_l \cdot \mathbf{n}_l \right] \Delta S_l, \tag{49}$$

where the subscript c denotes the cell-averaged variable located at cell center \mathbf{x}_c , the subscript l denotes the faced-averaged variable located at face center \mathbf{x}_l and $\boldsymbol{\pi}_l$ represents the viscous stress recovered from the nonequilibrium part. Considering the summation of force distributions in Eq. (26), the discrete momentum equation becomes

$$[\rho_c \mathbf{u}_c]^{n+1} = [\rho_c \mathbf{u}_c]^n - \frac{\Delta t}{|V_c|} \sum_l^N \left[\rho_l \mathbf{u}_l \mathbf{u}_l \cdot \mathbf{n}_l + c_s^2 \rho_l \mathbf{n}_l - \boldsymbol{\pi}_l \cdot \mathbf{n}_l \right] \Delta S_l + \frac{\Delta t}{2} (\mathbf{F}_c^n + \mathbf{F}_c^{n+1}), \tag{50}$$

where \mathbf{F}_c denotes the cell-averaged volumetric force.

Physically, the velocity field should be zero for a quiescent droplet system at the equilibrium state, at which Eq. (50) could be simplified to

$$\Delta t \mathbf{F}_c - \frac{\Delta t}{|V_c|} \sum_l^N c_s^2 \rho_l \mathbf{n}_l \Delta S_l = 0. \tag{51}$$

Eq. (51) can be viewed as the discretization of the following equation:

$$\mathbf{F} - \nabla \left(\rho c_s^2 \right) = 0, \tag{52}$$

which corresponds exactly to the continuum pressure tensor defined by Eq. (35). As Eq. (52) is practically solved by Eq. (51), an addition term \mathbf{S} will be introduced due to the discretization. According to Eq. (21), the face density ρ_l is obtained from the zeroth moment of \bar{f} , which in turn is evaluated by Eq. (15). For a quiescent droplet system at the equilibrium state, both \bar{f} and \bar{f}^+ would be reduced to f^E . Taking the zero velocity condition into consideration, the face density ρ_l can be viewed as being directly reconstructed from the adjacent cell densities via the corresponding scheme defined by Eq. (17) or (18).

For the face-based reconstruction scheme utilized in current research, Eq. (51) turns into

$$\Delta t \mathbf{F}_c - \frac{\Delta t}{2|V_c|} \sum_l^4 c_s^2 \rho_c \mathbf{n}_l \Delta S_l - \frac{\Delta t}{2|V_c|} \sum_l^4 c_s^2 \rho_{cl} \mathbf{n}_l \Delta S_l = 0, \tag{53}$$

where ρ_{cl} indicates the averaged density of cell V_{cl} that is adjacent to surface element ΔS_l . Mindful that $\Delta S_l = 1$ and $|V_c| = 1$ for the Cartesian mesh, Eq. (53) can be further simplified as

$$\Delta t \mathbf{F}_c = \Delta t c_s^2 \frac{\rho(\mathbf{x}_c + \Delta \mathbf{l}) - \rho(\mathbf{x}_c - \Delta \mathbf{l})}{2}, \tag{54}$$

where $\Delta \mathbf{l} = (0, \Delta x)$ or $(\Delta x, 0)$. Apparently, the gradient of density is computed by a central difference scheme which lacks the property of isotropy. Hence, nonisotropic interface will be produced by DUGKS employing the central difference face-based reconstruction scheme.

For the cell-based reconstruction scheme, the face density ρ_l is reconstructed by replacing the distribution function \bar{f}^+ in Eq. (18) with the equilibrium distribution f^E and taking the summation of i . For convenience, the derivative terms are packed into $O(\Delta x)$. The face density ρ_l then can be estimated by

$$\rho_l = \frac{1}{3}(\rho_c + \rho_{cl}) + \frac{1}{6}\rho_c + \frac{1}{6}\rho_{cl} + O(\Delta x). \tag{55}$$

Substituting the above equation into Eq. (51) will eventually result in Eq. (54), which indicates a nonisotropic discretization of $\nabla\rho$. Hence, nonisotropic interface will be similarly generated by DUGKS employing the cell-based reconstruction scheme.

5.2 The lattice Boltzmann method

The evolution equation solved by LB method reads

$$\tilde{f}(\mathbf{x} + \Delta\mathbf{x}, t_n + \Delta t) = \tilde{f}^n(\mathbf{x}) + \frac{2\Delta t}{2\tau + \Delta t} [f^{E,n}(\mathbf{x}) - \tilde{f}^n(\mathbf{x})] + \frac{2\tau \Delta t}{2\tau + \Delta t} f^{S,n}(\mathbf{x}), \quad (56)$$

where

$$\tilde{f} = f - \frac{\Delta t}{2} \Omega - \frac{\Delta t}{2} f^{S,n}. \quad (57)$$

The equilibrium distribution function f^E is evaluated via Eq. (4). The force distribution function f^S is evaluated by Eq. (25). The conservative variables are calculated by

$$\rho = \sum_i \tilde{f}_i, \rho \mathbf{u} = \sum_i \tilde{f}_i \xi_i + \frac{\Delta t}{2} \mathbf{F}_s, \quad (58)$$

where F_s denotes the interaction force defined by Eq. (29). The time step Δt has an identical value of the grid spacing Δx , which remains 1.0 in current research. The parameter α also holds a constant value of 1.0.

Acknowledgements

This article is particularly written in memory of Dr. Wang Peng, who spotted the nonisotropic problem of pseudopotential-based DUGKS and offered helpful ideas to overcome it. We appreciate a lot of his suggestions. This work is supported by the high performance computing power and technical support provided by Xi'an Future Artificial Intelligence Computing Center.

Authors' contributions

Zeren Yang: Methodology, Software, Validation, Formal analysis, Data Curation, Writing - Original draft preparation. Sha Liu: Funding acquisition, Methodology, Writing - Review and Editing. Congshan Zhuo: Supervision, Funding acquisition, Resources, Investigation, Writing - Review and Editing. Chengwen Zhong: Project administration, Funding acquisition, Conceptualization, Writing - Reviewing and Editing. All authors read and approved the final manuscript.

Funding

This study is sponsored by the National Numerical Wind Tunnel Project, the National Natural Science Foundation of China (No. 11902266, 11902264, 12072283), and the 111 Project of China (B17037).

Availability of data and materials

The data that support the findings of this study are available from the corresponding author upon reasonable request.

Declarations

Competing interests

The authors declare that they have no competing interests.

Received: 30 June 2022 Accepted: 26 August 2022

Published online: 19 September 2022

References

- Osher S, Sethian JA (1988) Fronts propagating with curvature-dependent speed: Algorithms based on Hamilton-Jacobi formulations. *J Comput Phys* 79(1):12–49
- Hirt CW, Nichols BD (1981) Volume of fluid (VOF) method for the dynamics of free boundaries. *J Comput Phys* 39(1):201–225
- Jacqmin D (1999) Calculation of two-phase Navier-Stokes flows using phase-field modeling. *J Comput Phys* 155(1):96–127

4. Fan Y, Fang J, Bolotnov I (2021) Complex bubble deformation and break-up dynamics studies using interface capturing approach. *Exp Comput Multiph Flow* 3(3):139–151
5. Guo Z, Zheng C, Shi B (2011) Force imbalance in lattice Boltzmann equation for two-phase flows. *Phys Rev E* 83:036707
6. Liu H, Wu L, Ba Y, Xi G, Zhang Y (2016) A lattice Boltzmann method for axisymmetric multicomponent flows with high viscosity ratio. *J Comput Phys* 327:873–893
7. Wen B, Zhou X, He B, Zhang C, Fang H (2017) Chemical-potential-based lattice Boltzmann method for nonideal fluids. *Phys Rev E* 95:063305
8. Li Q, Luo KH, Kang QJ, He YL, Chen Q, Liu Q (2016) Lattice Boltzmann methods for multiphase flow and phase-change heat transfer. *Prog Energy Combust Sci* 52:62–105
9. Geier M, Fakhari A, Lee T (2015) Conservative phase-field lattice Boltzmann model for interface tracking equation. *Phys Rev E* 91:063309
10. Yang K, Guo Z (2016) Lattice Boltzmann method for binary fluids based on mass-conserving quasi-incompressible phase-field theory. *Phys Rev E* 93:043303
11. Gunstensen AK, Rothman DH, Zaleski S, Zanetti G (1991) Lattice Boltzmann model of immiscible fluids. *Phys Rev A* 43:4320–4327
12. He X, Shan X, Doolen GD (1998) Discrete Boltzmann equation model for nonideal gases. *Phys Rev E* 57:R13–R16
13. Swift MR, Osborn WR, Yeomans JM (1995) Lattice Boltzmann simulation of nonideal fluids. *Phys Rev Lett* 75:830–833
14. Shan X, Chen H (1993) Lattice Boltzmann model for simulating flows with multiple phases and components. *Phys Rev E* 47:1815–1819
15. Yu Z, Fan LS (2009) An interaction potential based lattice Boltzmann method with adaptive mesh refinement (AMR) for two-phase flow simulation. *J Comput Phys* 228(17):6456–6478
16. Huang H, Krafczyk M, Lu X (2011) Forcing term in single-phase and Shan-Chen-type multiphase lattice Boltzmann models. *Phys Rev E* 84:046710
17. Hu A, Li L, Chen S, Liao Q, Zeng J (2013) On equations of state in pseudo-potential multiphase lattice Boltzmann model with large density ratio. *Int J Heat Mass Transf* 67:159–163
18. Wu Y, Gui N, Yang X, Tu J, Jiang S (2018) Fourth-order analysis of force terms in multiphase pseudopotential lattice Boltzmann model. *Comput Math Appl* 76(7):1699–1712
19. He X, Doolen GD (2002) Thermodynamic foundations of kinetic theory and lattice Boltzmann models for multiphase flows. *J Stat Phys* 107:309–328
20. Benzi R, Biferale L, Sbragaglia M, Succi S, Toschi F (2006) Mesoscopic modeling of a two-phase flow in the presence of boundaries: The contact angle. *Phys Rev E* 74:021509
21. Sbragaglia M, Benzi R, Biferale L, Succi S, Sugiyama K, Toschi F (2007) Generalized lattice Boltzmann method with multirange pseudopotential. *Phys Rev E* 75:026702
22. Shan X (2008) Pressure tensor calculation in a class of nonideal gas lattice Boltzmann models. *Phys Rev E* 77:066702
23. Kupershtokh AL, Medvedev DA, Karpov DI (2009) On equations of state in a lattice Boltzmann method. *Comput Math Appl* 58(5):965–974
24. Sbragaglia M, Shan X (2011) Consistent pseudopotential interactions in lattice Boltzmann models. *Phys Rev E* 84:036703
25. Li Q, Luo KH, Li XJ (2012) Forcing scheme in pseudopotential lattice Boltzmann model for multiphase flows. *Phys Rev E* 86:016709
26. Huang R, Wu H (2016) Third-order analysis of pseudopotential lattice Boltzmann model for multiphase flow. *J Comput Phys* 327:121–139
27. Chen L, Kang Q, Mu Y, He YL, Tao WQ (2014) A critical review of the pseudopotential multiphase lattice Boltzmann model: Methods and applications. *Int J Heat Mass Transf* 76:210–236
28. Guo Z, Xu K, Wang R (2013) Discrete unified gas kinetic scheme for all Knudsen number flows: Low-speed isothermal case. *Phys Rev E* 88:033305
29. Guo Z, Wang R, Xu K (2015) Discrete unified gas kinetic scheme for all Knudsen number flows. II. Thermal compressible case. *Phys Rev E* 91:033313
30. Liu H, Kong M, Chen Q, Zheng L, Cao Y (2018) Coupled discrete unified gas kinetic scheme for the thermal compressible flows in all Knudsen number regimes. *Phys Rev E* 98:053310
31. Zhong M, Zou S, Pan D, Zhuo C, Zhong C (2021) A simplified discrete unified gas-kinetic scheme for compressible flow. *Phys Fluids* 33(3):036103
32. Wen X, Wang LP, Guo Z, Shen J (2021) An improved discrete unified gas kinetic scheme for simulating compressible natural convection flows. *J Comput Phys X* 11:100088
33. Bo Y, Wang P, Guo Z, Wang LP (2017) DUGKS simulations of three-dimensional Taylor–Green vortex flow and turbulent channel flow. *Comput Fluids* 155:9–21
34. Zhang R, Zhong C, Liu S, Zhuo C (2020) Large-eddy simulation of wall-bounded turbulent flow with high-order discrete unified gas-kinetic scheme. *Adv Aerodyn* 2(1):26
35. Chen T, Wen X, Wang LP, Guo Z, Wang J, Chen S (2020) Simulation of three-dimensional compressible decaying isotropic turbulence using a redesigned discrete unified gas kinetic scheme. *Phys Fluids* 32(12):125104
36. Tao S, Zhang H, Guo Z, Wang LP (2018) A combined immersed boundary and discrete unified gas kinetic scheme for particle–fluid flows. *J Comput Phys* 375:498–518
37. Huo Y, Rao Z (2018) The discrete unified gas kinetic scheme for solid-liquid phase change problem. *Int Commun Heat Mass Transf* 91:187–195
38. Wang Y, Zhong C, Liu S (2019) Arbitrary Lagrangian–Eulerian-type discrete unified gas kinetic scheme for low-speed continuum and rarefied flow simulations with moving boundaries. *Phys Rev E* 100:063310
39. Zhang Y, Zhu L, Wang R, Guo Z (2018) Discrete unified gas kinetic scheme for all Knudsen number flows. III. Binary gas mixtures of Maxwell molecules. *Phys Rev E* 97:053306

40. Zhang A, Guo Z, Wang Q, Xiong S (2019) Three-dimensional numerical simulation of bubble rising in viscous liquids: A conservative phase-field lattice-Boltzmann study. *Phys Fluids* 31(6):063106
41. Zhu L, Guo Z (2017) Numerical study of nonequilibrium gas flow in a microchannel with a ratchet surface. *Phys Rev E* 95:023113
42. Liu H, Cao Y, Chen Q, Kong M, Zheng L (2018) A conserved discrete unified gas kinetic scheme for microchannel gas flows in all flow regimes. *Comput Fluids* 167:313–323
43. Luo XP, Wang CH, Zhang Y, Yi HL, Tan HP (2018) Multiscale solutions of radiative heat transfer by the discrete unified gas kinetic scheme. *Phys Rev E* 97:063302
44. Song X, Zhang C, Zhou X, Guo Z (2020) Discrete unified gas kinetic scheme for multiscale anisotropic radiative heat transfer. *Adv Aerodyn* 2(1):3
45. Guo Z, Xu K (2021) Progress of discrete unified gas-kinetic scheme for multiscale flows. *Adv Aerodyn* 3(1):6
46. Zhang C, Yang K, Guo Z (2018) A discrete unified gas-kinetic scheme for immiscible two-phase flows. *Int J Heat Mass Transf* 126:1326–1336
47. Yang Z, Zhong C, Zhuo C (2019) Phase-field method based on discrete unified gas-kinetic scheme for large-density-ratio two-phase flows. *Phys Rev E* 99:043302
48. Yang Z, Liu S, Zhuo C, Zhong C (2022) Conservative multilevel discrete unified gas kinetic scheme for modeling multiphase flows with large density ratios. *Phys Fluids* 34(4):043316
49. Zeng W, Zhang C, Guo Z (2022) Well-balanced discrete unified gas-kinetic scheme for two-phase systems. *Phys Fluids* 34(5):052111
50. Guo Z (2021) Well-balanced lattice Boltzmann model for two-phase systems. *Phys Fluids* 33(3):031709
51. Wang P, Zhu L, Guo Z, Xu K (2015) A comparative study of LBE and DUGKS methods for nearly incompressible flows. *Commun Comput Phys* 17(3):657–681
52. Wang P, Wang LP, Guo Z (2016) Comparison of the lattice Boltzmann equation and discrete unified gas-kinetic scheme methods for direct numerical simulation of decaying turbulent flows. *Physical Review E*. 94:043304
53. Yang Z, Zhong C, Zhuo C, Liu S (2022) Spatio-temporal error coupling and competition in meso-flux construction of discrete unified gas-kinetic scheme. *Comput Fluids* 244:105537
54. Kumar A (2004) Isotropic finite-differences. *J Comput Phys* 201(1):109–118
55. Li Q, Luo KH, Li XJ (2013) Lattice Boltzmann modeling of multiphase flows at large density ratio with an improved pseudopotential model. *Phys Rev E* 87:053301
56. Li Q, Yu Y, Huang RZ (2021) Achieving thermodynamic consistency in a class of free-energy multiphase lattice Boltzmann models. *Phys Rev E* 103:013304
57. Zhu L, Guo Z, Xu K (2016) Discrete unified gas kinetic scheme on unstructured meshes. *Comput Fluids* 127:211–225

Publisher's Note

Springer Nature remains neutral with regard to jurisdictional claims in published maps and institutional affiliations.

Submit your manuscript to a SpringerOpen[®] journal and benefit from:

- Convenient online submission
- Rigorous peer review
- Open access: articles freely available online
- High visibility within the field
- Retaining the copyright to your article

Submit your next manuscript at ► [springeropen.com](https://www.springeropen.com)
